Intermediate flexural detachment in FRP-plated concrete beams through a 3D mechanism-based regularized eXtended Finite Element Method

Elena Benvenuti*, elena.benvenuti@unife.it, Dipartimento di Ingegneria, Università di Ferrara, via Saragat 1, I-44122 Ferrara, Italy
Nicola Orlando nicola.orlando@unife.it, Dipartimento di Ingegneria, Università di Ferrara, via Saragat 1, I-44122 Ferrara, Italy

Abstract

The present study focuses on a three-dimensional computational methodology aimed at modeling the detachment of FRP plates from reinforced concrete beams. Most finite element models introduce FRP-to-concrete bond-slip laws difficult to be derived, while simulate the cracks in the concrete with smeared crack models. Conversely, the proposed approach is based on the regularized eXtended Finite Element Method with a mechanism-based detachment. It does not require bond-slip laws, and makes use of standard material parameters. The introduction of a regularization length and the adoption of a proper mechanical framework lead to an accurate and predictive methodology for smooth simulations of the FRP-detachment process. In the currently investigated range of thicknesses and widths of the FRP plate, the proposed methodology discloses the dominance of detachment by intermediate flexural cracks.

Keywords: FRP-reinforcements, bending test, debonding, XFEM

1. Introduction

In the last twenty years, FRP plates have been commonly used to increase the structural strength and delay the ultimate failure-load of concrete beams. Based on a three-dimensional regularized eXtended Finite Element Method with a mechanism-based detachment, the present approach provides a reliable and

complete picture of the circumstances under which FRP plated beams typically fail.

Since the 1990s, experimental tests and numerical analyses have been intensively investigating the strengthening effect induced by FRP plates externally bonded to concrete beams, proving their suitability for the rehabilitation of engineering structures [1, 2]. Experiments show that failure of FRP-plated concrete beams is brittle and occurs as a consequence of the detachment of the FRP plate from the concrete support [3, 4, 5, 6]. Though interfacial debonding at the interface between the FRP plate and the adhesive layer has been reported, in most cases, a thin layer comprehensive of the FRP plate, the adhesive layer and a thin concrete-cover detaches from the beam[3, 7, 8]. The FRP plate detachment can occur through different mechanisms, the most typical ones being displayed in Fig. 1. For instance, in the intermediate-crack-induced interfacial debonding, also referred to as shear-flexural or intermediate detachment, detachment propagates from a region of high stress concentration, such as flexural or shear cracks, towards the plate end, as shown in Fig. 1a. In the plate end debonding of Fig. 1b, detachment propagates from the plate end towards the midspan, often after concrete cover separation at the level of the longitudinal steel rebars[3, 9]. While plate end detachment is more typical of steel-plated beams [10], shear-flexural detachment represents the dominant failure mechanism for FRP-plated concrete beams [3, 7, 11, 12], especially for comparatively long bonding lengths [13].

The development of analytical and computational models of the FRP plate detachment from reinforced concrete beams is a complex task. Analytical models compute shearing and normal stresses at the interface between the beam and the FRP plate by imposition of the equilibrium and compatibility conditions [14, 15, 9, 4]. Among the available analytical models, the so-called bond-

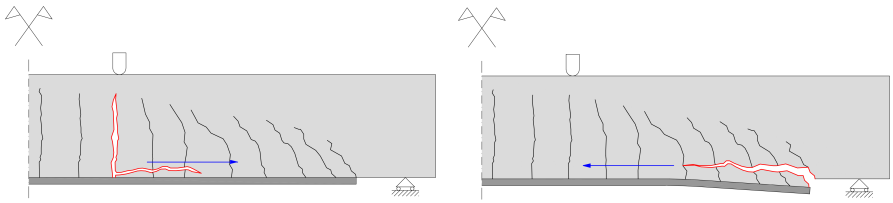

a) Intermediate crack debonding b) Plate end separation/debonding

Figure 1: The main failure modes by FRP-detachment

slip models [16] typically underestimate the importance of peeling stresses. This underestimate contrasts with what observed in single-lap shear tests on concrete blocks [17, 18], where the values of peeling stresses are significant. Analytical interface laws are often implemented in Finite Element (FE) models. In particular, FE models simulate the surface of detachment either through discrete cracks along the element edges [19, 20, 21], or cohesive-crack laws [22, 23, 24]. Discrete crack models aim at simulating only dominant cracks. Their main drawbacks are mesh bias and the necessity of mesh adaptation [25]. On the other hand, cohesive-crack laws rule the traction-separation law of the surface of detachment. For the simulation of the debonding of FRP plates, interface elements analogous to cohesive laws have been adopted along the FRP-concrete interface. Most literature studies model the FRP-concrete interface by means of bond-slip laws obtained from pull tests on FRP-to-concrete joints [16, 26]. However, effective bond-slip laws require the knowledge of the fracture energy, the identification of model parameters of difficult determination, and depend on the actual debonding mechanism [13]. Furthermore, loss of convergence of existing FE models is quite common [27]. As for concrete, cracks are typically modeled through smeared cracks [28] and crack-band models [29, 30, 31, 12, 32]. The latter overcome the primal mesh-dependency inherent to the originally proposed smeared crack models by relating the smallest finite element size to the fracture energy [33]. However, both smeared crack and crack-band models distort and

spread crack patterns [25]. Moreover, scaling the finite element size with the fracture energy introduces a secondary mesh-size dependency.

With respect to discrete crack models, where the discontinuities have to be aligned along the finite element edges, the so-called enriched FE models, such as the Generalized Finite Element Method (GFEM) [34, 35] and the eXtended Finite Element Method (XFEM) [36, 37, 38], embed the discontinuity within the finite elements by defining additional nodal degrees of freedom. Based on the partition of unity property of standard shape functions, GFEM and XFEM enrich the standard space of the shape functions with additional functions featuring the shape of the expected displacement field. Examples are the Heaviside function for displacement jumps and the asymptotic crack tip functions for cracks [39]. XFEM can also easily accommodate cohesive-crack laws [40, 41] and discrete cracks [42].

Developed by the authors in previous studies [41, 43, 44], the regularized XFEM method is a special variant of the XFEM fully suited to the modeling of the debonding failure of FRP-strengthened reinforced concrete beams. Unlike most FE models, where the interfacial stresses normal to the FRP-concrete interface are neglected [26], the present mechanism-based approach takes into account normal and shearing stresses, and can reproduce both shear/flexural cracks detachment and plate end separation. In the present study, concrete is modeled as an elasto-damaging material with a softening stress-strain law. The mesh-dependency of FE codes in the presence of softening constitutive laws is well known since the 1980s. This mesh-dependency is ascribed to the fact that the strain tends to localize into the narrowest possible finite element with the consequence that the structural path becomes mesh-size dependent. Correspondingly, the detection of mesh-dependency has spurred the development of non-local damage models [45, 46, 47], whose main merit is the introduction

of an additional characteristic length acting as a strain localization limiter. In fact, smeared crack, crack-band, and non-local models introduce an additional characteristic length into the modeling. In a pure mode I loading, the adoption of smeared crack models or non-local models is necessary to get mesh-size objective results. However, according to authors' experience [18, 48], when the aim is the simulation of the structural behavior of FRP-plated concrete beams, it is the detachment rather then the concrete cracking that needs to be regularized. Therefore, this rules out the real necessity of non-local or smeared crack models for the concrete bulk.

In the present methodology, the detachment of the cover made of the FRP plate and a thin concrete layer is localized within a volume. This volume tends to the surface of detachment for vanishing value of a regularization length. First, the displacement field is assumed to exhibit a regularized jump across the limit surface of detachment. This assumption introduces an additional length that describes the thickness of the detachment zone. Then, a suitable constitutive law is adopted for the detachment zone that allows for both shear/flexural-cracks-induced and plate end detachment. Finally, a continuous-discontinuous transition procedure is activated in the concrete elements that are crossed by the surface of detachment. It is recalled that XFEM procedures based on a regularized kinematics, however, completely different from the present one, have been applied to delamination in composite laminates [49, 50]. The role of size effects in the failure of FRP-strengthened beams has been recently investigated through a high order 1D XFEM based on a layered beam theory with high order kinematic relations [51].

The main novelty of the present study consists in the introduction of an additional regularization length that controls the width of the process zone and ensures a smooth continuous-discontinuous transition like non-local and smeared-

crack models, but without spreading the fracture zone. Moreover, unlike existing FE models based on bond-slip (interfacial) laws of difficult identification, the proposed regularized XFEM formulation requires few physically-consistent material parameters and gets the same results as discrete crack models without the need of mesh adaptation.

The mechanism-based regularized XFEM has succeeded in modeling single-shear lap tests [18, 52] and three point bending tests carried out on steel-fibre-reinforced concrete beams [48]. The present study applies for the first time the proposed methodology to FRP-strengthened reinforced concrete beams. What makes the present application different from the previous authors' publications on the mechanism-based regularized XFEM is the fact that it accounts for the interplay between the strengths of the concrete, the FRP plate and the steel rebars.

2. FRP detachment by means of the regularized XFEM approach

This section describes the kinematics of the regularized XFEM, the constitutive laws, and the damage evolution laws embedded in the continuous-discontinuous transition procedure. Specific subsections are devoted to the evolution of the damage in the concrete and the degradation of the mechanical properties of the steel.

2.1. Kinematics

Experiments suggest that the FRP reinforcement detaches together with the adhesive layer and a thin concrete substrate, while the surface of detachment $\mathcal{S}$ is roughly parallel to the FRP plate [3]. Across the surface of detachment, the displacement vector field $\mathbf{u}$ exhibits a jump $[\![\mathbf{u}]\!] = \mathbf{u}^+ - \mathbf{u}^-$. Accordingly, in the standard XFEM framework [36, 39, 37, 38, 53], the displacement field is

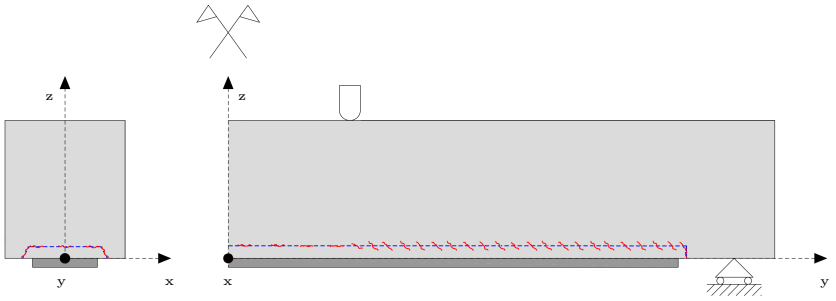

Figure 2: Qualitative scheme of the cracks distributed in the detachment zone

approximated as

$$\mathbf{u}^{st} = \mathbf{NU} + \mathcal{H}\mathbf{NA}\,, \tag{1}$$

where the Heaviside function $\mathcal{H}$ takes the values ± 1 across the discontinuity surface. In Eq. (1), matrix $\mathbf{N}$ contains the classic finite element interpolation functions, vector $\mathbf{U}$ collects the standard displacement degrees of freedom, and vector $\mathbf{A}$ gathers the additional degrees of freedom representative of the nodal displacement jumps.

2.2. A mechanism-based detachment mode

Basically, the surface of detachment results from the coalescence of meso-cracks developing in the concrete along a direction almost orthogonal to the direction $\mathbf{n}_f$ of the maximum principal tensile stress [54, 13]. In mixed-mode loadings, these meso-cracks are not orthogonal to the macro-surface of detachment [55, 13]. A possible qualitative picture of the expected meso-cracks developing in the detachment zone for the expected detachment mode is displayed in Fig. 2. In the mechanism-based regularized XFEM, the knowledge of the vector field $\mathbf{n}_f$ is crucial to the computation of the stress fields, as explained in Sec. 2.3. To this purpose, the directions of the expected meso-cracks is assumed, and, thus, the vector $\mathbf{n}_f$ is taken perpendicular to the directions of the

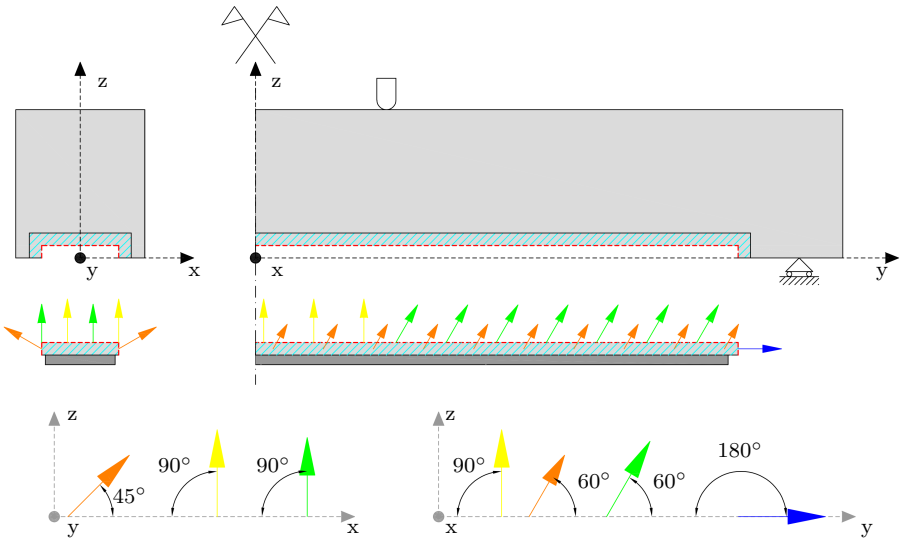

Figure 3: Scheme of the vectors $\mathbf{n}_f$ for the mechanism-based detachment

assumed meso-cracks. This way, the computation of the principal stresses at each integration points is avoided, and $\mathbf{n}_f$ becomes a sort of model parameter, that allows to unblock the detachment of the enriched layer. Fig. 3 shows the field of vector fields $\mathbf{n}_f$ above the FRP plate in the detachment zone. The different directions of $\mathbf{n}_f$ are highlighted with different colors. In particular, $\mathbf{n}_f$ between the loadings is aligned along the yellow (0, 0, 1) vectors. In the span from the loading point to the plate end, the direction of $\mathbf{n}_f$ coincides with that of the green (0, 1/2, $\sqrt{3}/2$) vectors. To allow for plate end detachment, at the back edge and along the side edges, $\mathbf{n}_f$ is aligned with vectors (0, 1, 0), in blue, and ($\sqrt{3}$, 1, $\sqrt{3}$), in orange, respectively.

2.3. Regularized XFEM

In the regularized XFEM approach, the surface of detachment is replaced by a regularized discontinuity, as shown in Fig. 4. Let the regularized Heaviside

function $\mathcal{H}_\rho$ [41] be

$$\mathcal{H}_\rho(\bar{d}(\boldsymbol{x})) = \frac{1}{V_\rho}\int_0^{\bar{d}(\boldsymbol{x})} e^{-\frac{|\xi|}{\rho}}\, d\xi = \text{sign}(\bar{d}(\boldsymbol{x}))(1 - e^{-\frac{|\bar{d}(\boldsymbol{x})|}{\rho}})\,, \tag{2}$$

where V_ρ is the normalization volume and is equal to ρ [41]. The regularized function depends on the signed distance $\bar{d}(\mathbf{x})$ from the surface of detachment $\mathcal{S}$ of normal $\mathbf{n}$. The macro-surface of detachment is implicitly simulated as a level set function [56] of $\bar{d}(\mathbf{x})$. Based on the $\mathbf{n}_f$ vectors normal to the meso-cracks, whose mechanical meaning has been illustrated in subsection 2.2, the derivative of H_ρ with respect to $\mathbf{x}$ is approximated as

$$\nabla\mathcal{H}_\rho \approx \delta_\rho\, \mathbf{n}_f\,, \tag{3}$$

where $\delta_\rho = \|\nabla\mathcal{H}_\rho\|$. Fig. 5 shows the shape of $\mathcal{H}_\rho$ and the Dirac's delta shape of δ_ρ, for $\rho = 0.125$, 0.25, 0.5 mm. The red dashed line denotes the intersection of the surface of detachment. For vanishing value of the regularization parameter ρ, the function $\mathcal{H}_\rho$ tends to the standard Heaviside function $\mathcal{H}$. Because the support of the regularized functions $\mathcal{H}_\rho$ and δ_ρ is not compact, a truncated support of 40ρ has been adopted, neglecting the contribute from nodes with distances from $\mathcal{S}$ larger than 20ρ. This choice of the truncation length is based on previous accuracy studies [57].

Therefore, Eq. (1) is replaced by the regularized displacement field

$$\mathbf{u} = \mathbf{NU} + \mathcal{H}_\rho\mathbf{NA}\,. \tag{4}$$

Eq. (4) tends to $\mathbf{u}^{st}$ (1) for vanishing ρ.

Finally, the strain field is evaluated

$$\boldsymbol{\varepsilon} = \boldsymbol{\varepsilon}^{(1)} + \boldsymbol{\varepsilon}^{(2)}\,, \tag{5}$$

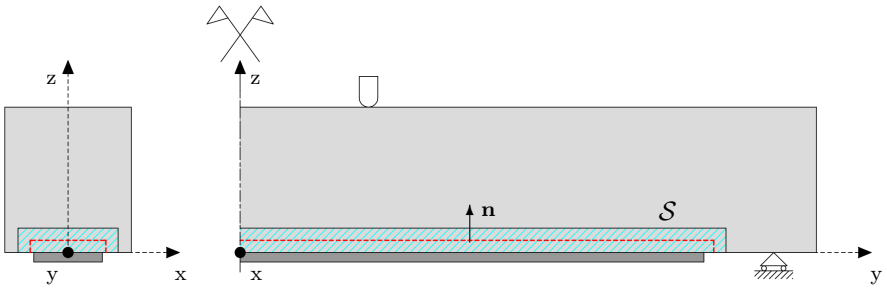

Figure 4: Qualitative picture of the detachment zone in the regularized XFEM

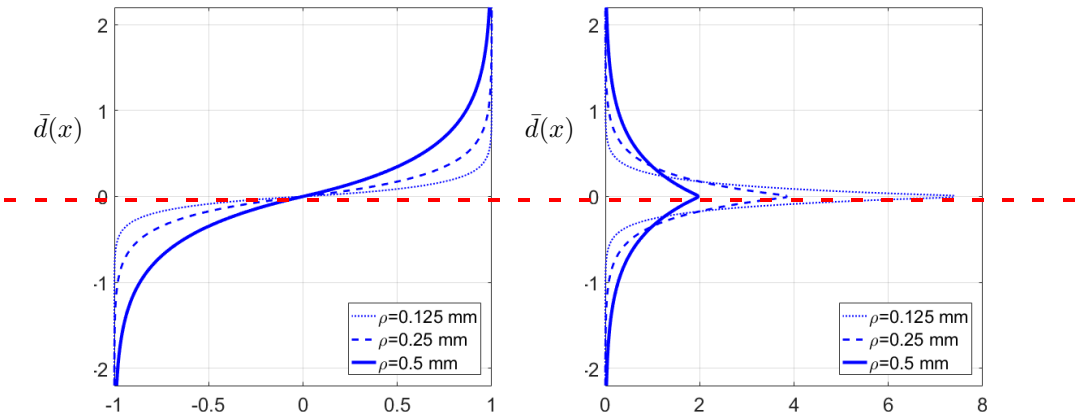

Figure 5: One-dimensional representation of the functions $\mathcal{H}_\rho$ (a) and δ_ρ (b); the red dashed line denotes the trace of the surface of detachment

where

$$\boldsymbol{\varepsilon}^{(1)} = \mathbf{B}\mathbf{U} + \mathcal{H}_\rho \mathbf{B}\mathbf{A}\,, \qquad \boldsymbol{\varepsilon}^{(2)} = \delta_\rho(\mathbf{N}\mathbf{A} \otimes \mathbf{n}_f)\,. \tag{6}$$

The field $\mathbf{n}_f$ is assumed based on the concept of mechanism-based detachment, as explained in the next section.

2.4. Concrete damage evolution and continuous-discontinuous transition

In the present work, concrete and steel are modeled with non-linear constitutive laws, while FRP and adhesive are modelled as elastic materials. As known, FRP plates should be modeled as orthotropic [15, 29]. However, because the fibers orientation of FRP plates used in the present applications is uniaxial and aligned with the loading direction, the FRP elastic modulus along the transverse direction is neglected, and the only longitudinal FRP elastic modulus is considered. This choice is quite common in the literature [30, 12, 32, 26, 32]. Moreover, concrete and steel have been modeled as isotropic materials. The damage evolution and the continuous/discontinuous transition procedure have been thoroughly discussed in previous references [58, 59]. In particular, an elasto-damage constitutive law is assumed for concrete, while the steel is governed by an elasto-plastic-damaging law. Moreover, perfect bond is assumed between steel bars and concrete.

The process of degradation of the mechanical properties of the concrete is controlled by two scalar isotropic damage variables, called $d^{(1)}$ and $d^{(2)}$. More precisely, the stress fields are computed as

$$\begin{aligned} \boldsymbol{\sigma}^{(1)} &= (1 - d^{(1)})\mathbf{E}\boldsymbol{\varepsilon}^{(1)} \quad \text{in the concrete}\,, \\ \boldsymbol{\sigma}^{(2)} &= (1 - d^{(2)})\mathbf{E}_c\boldsymbol{\varepsilon}^{(2)} \quad \text{in the detachment zone}\,. \end{aligned} \tag{7}$$

It was proved [41, 43] that, for consistency reasons, $\mathbf{E}_c$ has to be assumed equal to $\mathbf{E}/t\delta_\rho$, t being a unit dimensional parameter.

The variational formulation associated with the present regularized XFEM formulation has been thoroughly discussed in previous studies [41, 43, 44], that have shown that the stress $\boldsymbol{\sigma}^{(2)}$ must be coupled with the strain term $\boldsymbol{\varepsilon}^{(2)}$ and decoupled from $\boldsymbol{\varepsilon}^{(1)}$, in order to get mechanically consistent results. The complete derivation is omitted for the sake of brevity. The mechanical work is expressed as

$$\int_V \boldsymbol{\sigma}^{(1)} \cdot \boldsymbol{\varepsilon}^{(1)} + \boldsymbol{\sigma}^{(2)} \cdot \boldsymbol{\varepsilon}^{(2)} \, dV - \mathcal{L}_{ext} = 0 \,, \tag{8}$$

where $\mathcal{L}_{ext}$ is the external work.

A total-strain-driven damage format [60] is adopted, where the evolution of the damage ω is governed by the exponential Rankine law [61]

$$\omega = 1 - \frac{r_0}{\omega} \exp\left(-2H_s \, \frac{\omega - r_0}{r_0}\right), \tag{9}$$

where ω denotes either $d^{(1)}$ or $d^{(2)}$, and the threshold r_0 is equal to the tensile concrete strength f_{ctm} and H_s is a softening parameter.

The loading-unloading functions controlling the evolution of $d^{(1)}$ and $d^{(2)}$ are

$$\psi = \varsigma - r \leq 0 \,, \qquad \Delta\omega \geq 0 \,, \qquad \psi \Delta\omega = 0 \,, \tag{10}$$

where the scalar ς is an equivalent stress, and r is the current damage threshold. The constitutive law based on Eq. (9) is reported in Fig. 6a for the one-dimensional case when $f_t = 3$ MPa, $E = 30000$ MPa, and $H_s = 0.1$.

The damage $d^{(1)}$ pertaining to the bulk ranges from the value 0, for the sound material, to the damage activation threshold d_{cr}. Once $d^{(1)}$ has reached the value d_{cr} at least in one integration point of a finite element, there, the regularized discontinuity is activated. Then, $d^{(1)}$ switches to $d^{(2)}$, with $d^{(2)}$

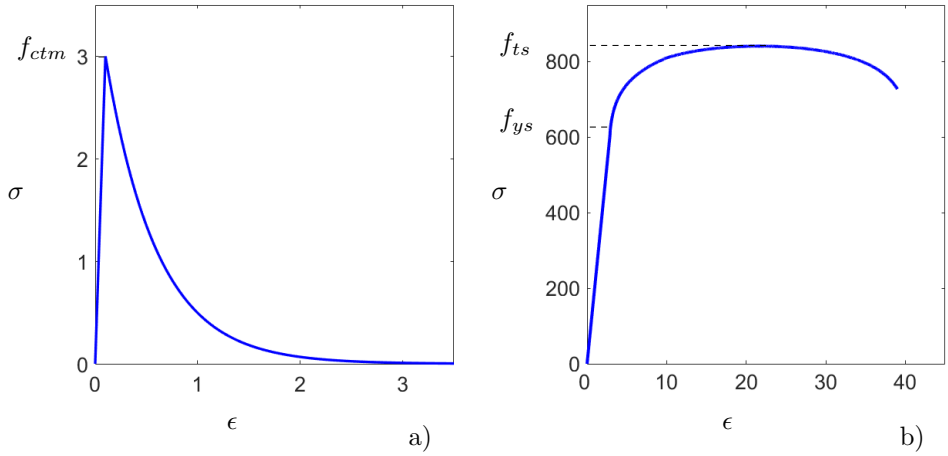

Figure 6: Qualitative one-dimensional representation of the damage laws adopted for the concrete matrix (a), with $f_{ctm} = 3$ MPa, $E = 30000$ MPa, H_s=0.1, and the steel rebars (b), with $K = 1200$, $n = 0.08$, $D^c = 0.98$, ϵ_d=0.01, and ϵ_r=0.04

assuming values from d_{cr} up to 1 for complete detachment. In synthesis,

$$d^{(1)} = \min\{d_{cr},\, \omega\}\,, \quad d^{(2)} = \max\{d_{cr},\, \omega\}\,, \tag{11}$$

where ω is computed through Eq. (9).

The computation of the equivalent stress scalar ς is different for concrete and regularized detachment zone. In the former, the stress that rules the evolution of $d^{(1)}$ is $\bar{\boldsymbol{\sigma}}^{(1)} = \mathbf{E}\,\mathbf{B}\mathbf{U}$; in the latter, the driving stress is computed as $\bar{\boldsymbol{\sigma}}^{(2)} = \mathbf{E}_c\,\delta_\rho(\mathbf{N}\mathbf{A}\otimes\mathbf{n})$. Let the principal stresses of $\bar{\boldsymbol{\sigma}}^{(1)}$ and $\bar{\boldsymbol{\sigma}}^{(2)}$ be $\{\bar{\sigma}_i^{(1)}\}$ and $\{\bar{\sigma}_i^{(2)}\}$, respectively, with $i = 1,\, 2,\, 3$. Then, the equivalent stress at the current state is computed as

$$\varsigma^{(1)} = \max\{\langle\bar{\sigma}_i^{(1)}\rangle\}\,, \qquad i = 1,\, 2,\, 3\,, \tag{12}$$

in the concrete, and

$$\varsigma^{(2)} = \max\{\langle\bar{\sigma}_i^{(2)}\rangle\}\,, \qquad i = 1,\, 2,\, 3\,, \tag{13}$$

in the regularized detachment zone, where the Macauley brackets $\langle\cdot\rangle$ select the

positive part of their argument $\cdot$.

Noteworthy, damage in compression is not taken into account. This restriction precludes detecting failure by concrete crushing.

2.5. Steel constitutive law

The non-linear behavior of steel is modeled through a well-known elasto-damaging law based on a modified version of Ramberg-Osgood's law for ductile plastic damage [62, 63]. For instance, in the one-dimensional case, the plastic strain ϵ_p and the steel damage d are related to the von Mises stress σ_{eq} trough

$$\epsilon_p = \left[\frac{\sigma_{eq}}{(1-d)K}\right]^{\frac{1}{n}}, \tag{14}$$

where K and n are material coefficients. In Eq. (14), ϵ_p and ϵ_R denote the one-dimensional strain at damage threshold and at failure, respectively. The intrinsic value of damage at failure D^c is assumed to be material properties [62]

$$\begin{cases} d = 0 & \epsilon_p \leq \epsilon_D \\ d = D^c \dfrac{\epsilon_p - \epsilon_D}{\epsilon_R - \epsilon_D} & \epsilon_D < \epsilon_p \leq \epsilon_R \\ d = D^c & \epsilon_p \geq \epsilon_R \end{cases} . \tag{15}$$

Fig. 6b displays a one-dimensional representation of the stress-strain of the steel for one-dimensional tension for $K = 1200$, $n = 0.08$, $D^c = 0.98$, ϵ_d=0.01, and ϵ_r=0.04.

3. Validation of the mechanism-based regularized XFEM

The present section presents the results obtained in the simulation of four point bending tests of FRP strengthened beams carried out on several beam geometries for both plated and unplated configurations [7, 8]. For the whole set

of simulations, the experimentally determined material properties have been adopted. In fact, the concrete elasto-damaging model and the continuous-discontinuous transition procedure require few model parameters that can be deduced from the producer's data. The values of the regularization parameters ρ, indicated in Tab.1, have been kept constant during the simulations. Considering that the computed thickness of the detachment zone turns out being 40ρ, ρ has been identified based on the experimental structural paths, and assuming a thickness of the detachment process zone of about $1-2$ cm. Noteworthy, for fixed ρ, the results of the present regularized XFEM formulation were previously shown to be independent of the mesh size [58].

The application of a local damage model usually leads to results dependent on the mesh employed. In a recent work [48], the mesh independence of the regularized XFEM approach has been proved for steel fiber reinforced concrete beams subjected to three point loading tests.

Based on the experimentally observed failure modes, the detachment surface has been placed in the middle of the concrete cover between the FRP plate and the steel bars.

To solve the incremental problem, an arc-length iterative procedure has been implemented in a 3D Fortran code developed by the authors [64]. The code is made fully available to the interested researchers.

3.1. Thick beam: geometry and material parameters

The experimental test performed by [8] has been modeled. It is based on the beam of Fig. 7a with l/h of about 5, and a shear span to depth ratio of 1.76.

The concrete material parameters are taken directly from the reference experimental data [8] and are collected in Tab. 1. Young's modulus and tensile strength were estimated through the expressions [65] $22000\,[f_{cm}/10]^{0.3} = 34360$ MPa and $0.30\,f_{cm}^{2/3} = 3.28$ MPa, respectively, with $f_{cm} = 44.2$ MPa.

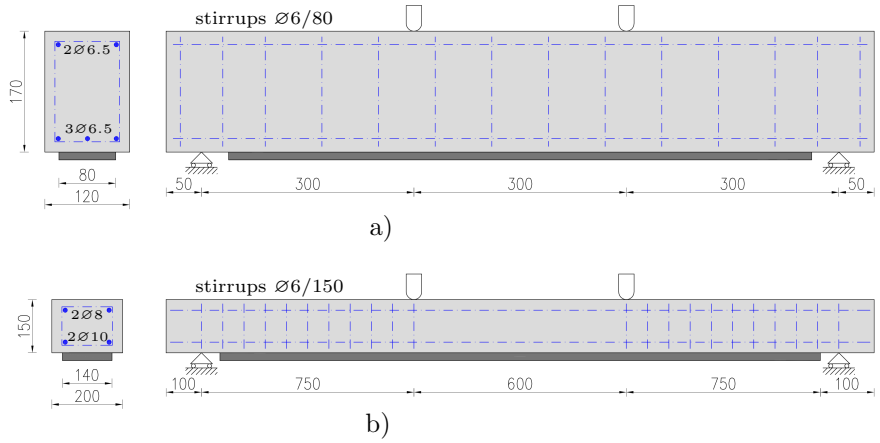

Figure 7: Geometry of the thick ($l/h \simeq 5$) and the thin ($l/h \simeq 15$) beams tested in [8] (a) and [7] (b), respectively

	Exp. set [8]	Exp. set [7]
E [MPa]	34360	25000
ν	0.2	0.2
f_{ctm} [MPa]	3.28	2.8
H_s	0.008	0.01
ρ [mm]	0.15	0.45
d_{cr} [mm]	0.999	0.999

Table 1: Mechanical properties and parameters of the concrete

	Exp. set [8]	Exp. set [7]—
E [MPa]	210000	210000
ν	0.3	0.3
f_{ts} [MPa]	765	575
K	1000	640
n	0.10	0.03
D^c	0.98	0.98
ϵ_D	0.020	0.005
ϵ_R	0.040	0.05

Table 2: Mechanical properties and parameters of the steel

	Exp. set [8]	Exp. set [7]
E_{FRP} [MPa]	240000	127000
ν_{FRP}	0.3	0.3
t_{FRP} mm	0.33	0.8
b_{FRP} mm	80	140

Table 3: Mechanical properties and geometry of the FRP plate

The material parameters and mechanical properties of the steel of the rebars and the FRP plate are gathered in Tabs. 2 and 3. To avoid an excessive mesh refinement, the FRP plate thickness has been taken equal to 2 mm. Consequently, an effective Young's modulus $\bar{E}_{FRP} = E_{FRP}\, t_{FRP}\, b_{FRP}/2$ has been set.

The mesh made of 109264 tetrahedral finite elements is shown in Fig. 8a. Only the first layer of finite elements above the FRP plate has been enriched. In the enriched layer, the characteristic mesh-size is 6 mm. To reduce the computational burden and exploit the symmetries of the beam, one quarter of the specimen has been modelled. The surface of detachment is in the concrete at a distance of 3 mm from the upper surface of the FRP plate. Furthermore, a regularization parameter equal to $\rho = 0.15$ mm has been adopted.

On an i7-5930K PC with 6 3.50 GHz cores, the numerical simulation of the complete structural path required almost 20 hours.

3.2. Thin beam: geometry and material parameters

The numerical model has been applied to the experimental test [7]. The geometry of the beam having $l/h \simeq 15$ and shear span to depth ratio of about 6, is shown in Fig. 7b. The material properties deduced from the experimental data are reported in Tabs. 1- 3.

A regularization length of $\rho = 0.45$ mm has been adopted leading to a regularized layer whose thickness includes three rows of enriched finite elements.

The mesh employed for numerical analysis, reported in Fig. 8b, is made of 243771 tetrahedra with a characteristic size of 6 mm in the most refined part. With the same processor used for the thick beam, the entire simulation run for 3 days. The simulation time is three times that of the previous test, because the number of enriched elements is three times larger as well, while the number

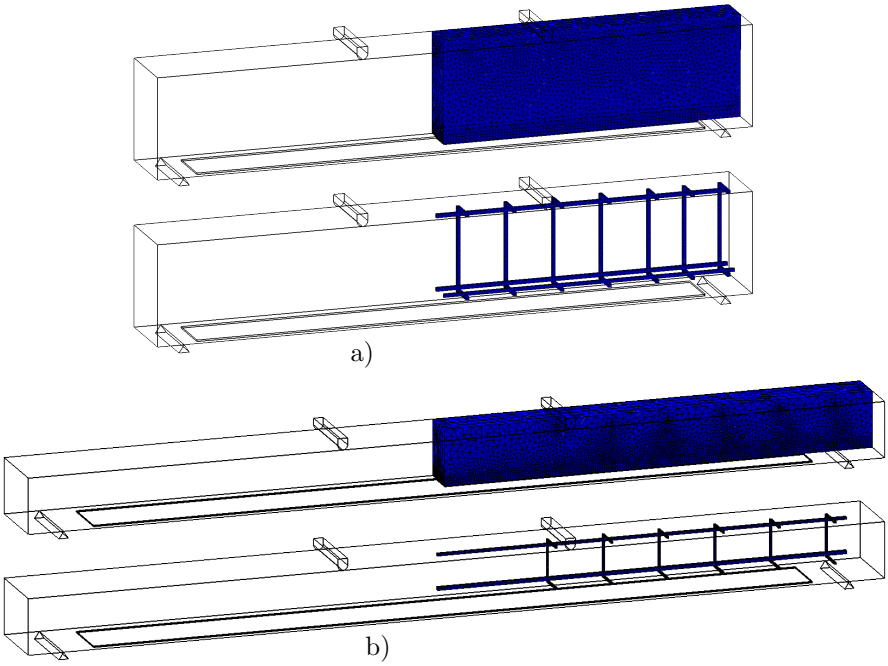

Figure 8: Meshes and details of the steel reinforcement for the two studied beams: a) 108354 elements with 70704 dofs for the beam tested in [8]; b) 243771 elements with 157809 dofs for the beam tested in [7]

of finite elements is doubled.

The surface of detachment has been imposed at a distance of 9 mm from the upper surface of the FRP plate.

3.3. Structural results

Fig. 9 displays the experimental and computed load-midspan-deflection curves for both the thick (a) and the thin (b) beam.

The post-detachment structural path of the thick beam exhibits a brittle drop and eventually joins the path of the control beam in the unplated configuration, up to exhaustion of the strength of the steel rebars. On the contrary, the failure of the thin beam is reached as soon as the FRP plate detaches, because the steel rebars had previously failed. In both the thin and the thick beam, in the first stage of the structural path, the response of the beams is almost elastic until the occurrence of the early cracks. Then, flexural and shear cracks develop within the concrete with subsequent loss of structural stiffness, while the progressive propagation of cracks increases the stress on the tensile steel rebars. In the last part of the structural response, the rebars gradually yield until failure. The gain in maximum load and stiffness obtained after application of the FRP plate is remarkable. The FRP reinforced systems shows higher performance on maximum load and flexural stiffness. However, failure changes from ductile to brittle. The experimental failure loads are properly estimated by the numerical procedure, with a discrepancy less than 6%.

3.4. Detachment mechanism

Detachment occurs by an intermediate flexural detachment mechanism. This can be deduced from Fig. 10, which displays the contour plots of the damage $d^{(1)}$ in the concrete matrix and in the steel reinforcements for three representative load steps of the test [8]. The early macro-cracks occur under the applied

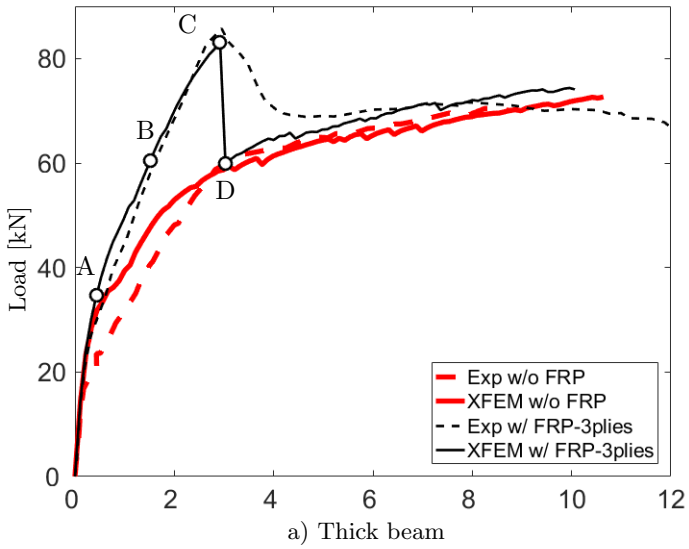

a) Thick beam

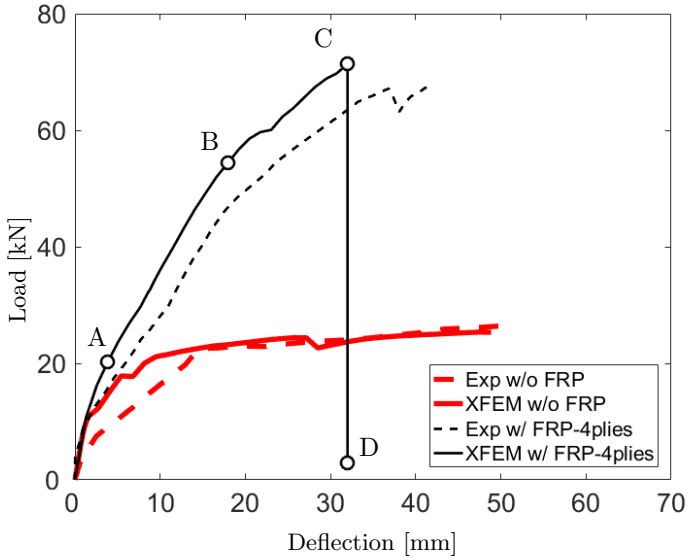

b) Slender beam

Figure 9: Comparison between experimental and numerical load-midspan-deflection curves for the beams tested in [8] (a) and [7] (b), respectively

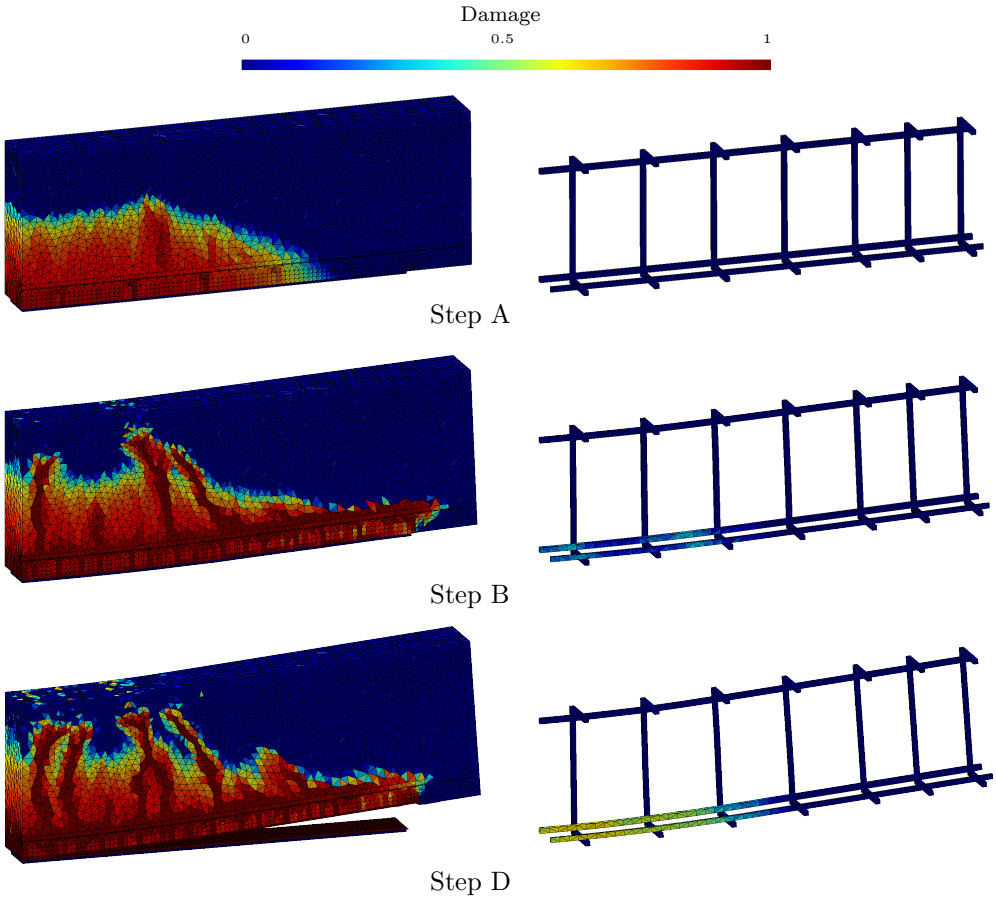

Figure 10: Contour plots of the damage $d^{(1)}$ at steps A, B and D of Fig. 9a for the thick beam tested in [8].

load (Step A). Then, cracks develop within the concrete bulk (Step B). The concrete damage starts at the midspan and propagates towards the plate end. At a certain distance from the plate end, the damage-front stops, and a new damage-front develops from the plate end to the beam midspan. Finally, the FRP plate fully detaches from the reinforced concrete beam in a single load step (Step D).

Fig. 11 illustrates the contour plots of the damage in the thin beam [7] over the detachment surface at steps A, C, and D. This confirms the same intermediate flexural cracking detachment mechanism already observed in the

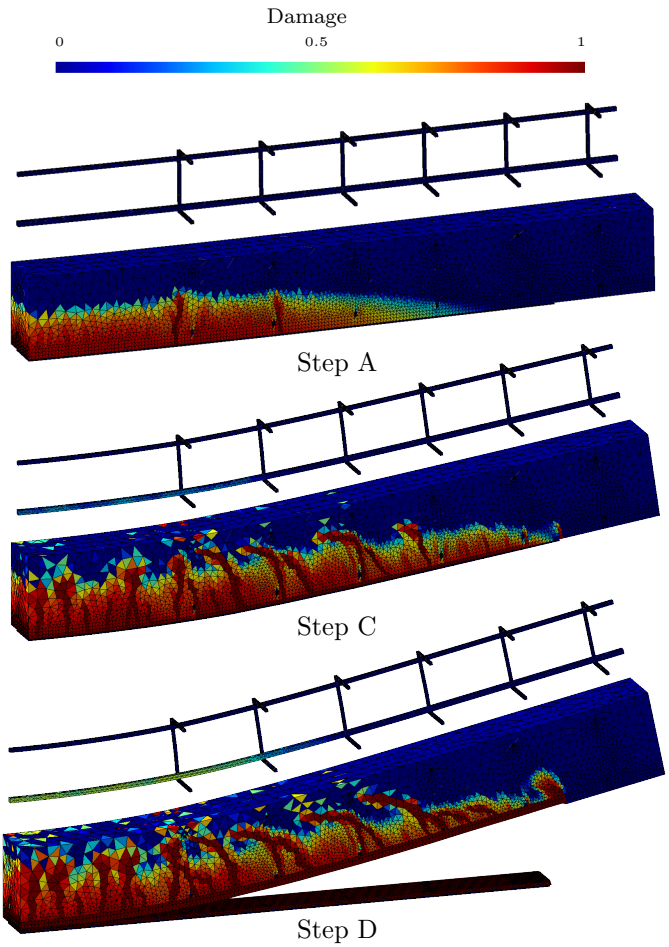

Figure 11: Contour Plots of the damage $d^{(1)}$ at steps A, C and D of Fig. 9b for the beam tested in [7]

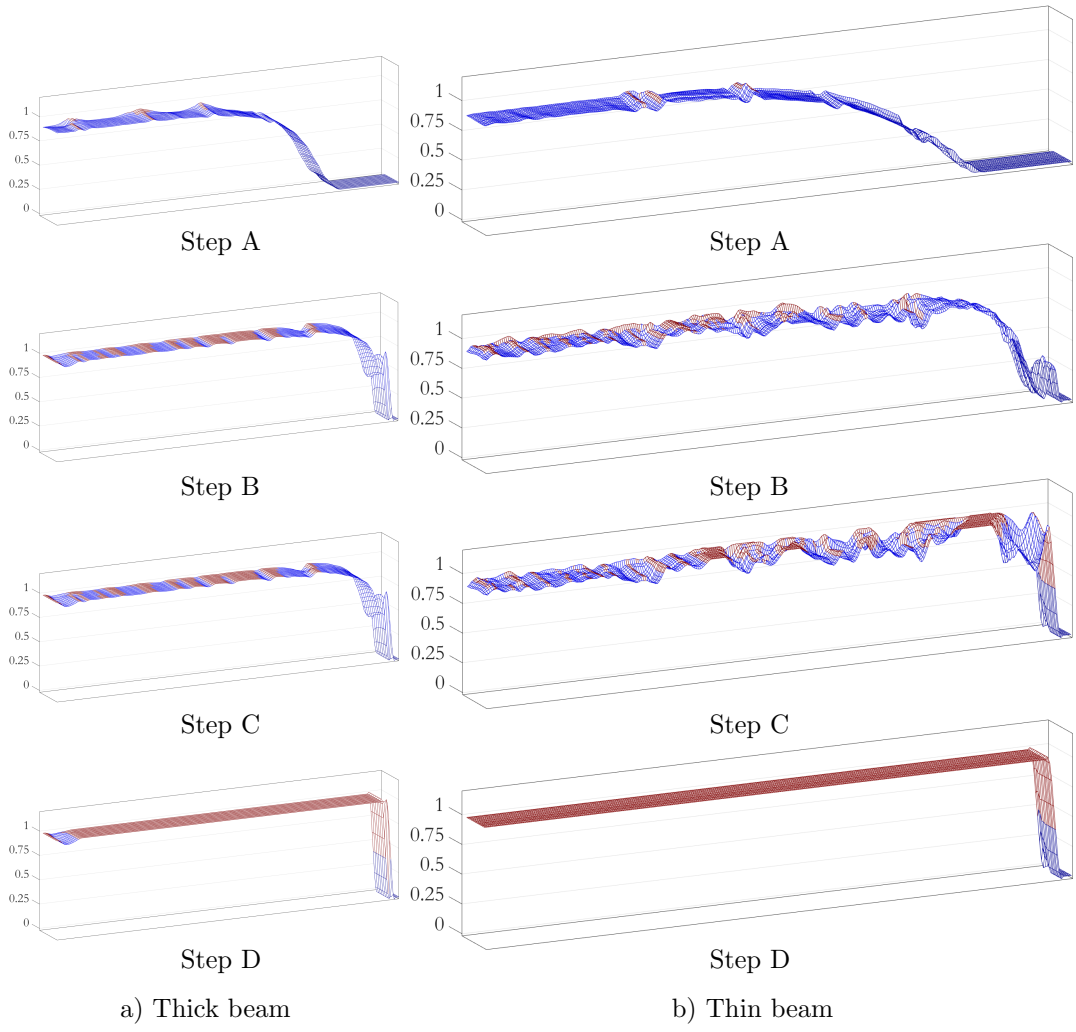

Figure 12: Damage $d^{(1)}$ evolution for the beams tested in [8] (a) and [7] (b), respectively, corresponding to stages A, B, C, and D of Fig. 9; the elements where the regularized XFEM has been activated are in red.

thick beam. On the right, the damage in the longitudinal rebars is shown to be localized at the flexural cracks.

The evolution of damage $d^{(1)}$ on the defined surface of detachment for both sets of experimental tests is shown in Fig. 12. The damage evolution starts from the midspan in the loaded area and propagates towards the plate end at step A. At a certain distance from the plate end, a secondary front of damage arises propagating from the plate end to the beam midspan (step B); failure and total detachment coincide and occurs at steps C-D. In this figure, the elements in red are those where the regularized XFEM has been activated.

4. Role of thickness and width of the FRP plate

To study the influence of the geometries of FRP reinforcement on the structural behavior of the beam, variable thicknesses and widths of the FRP plate have been considered. To the authors' knowledge, numerical studies of the influence of the FRP plate width b_{FRP} are only available for shear debonding of FRP sheets from concrete [66].

4.1. Structural effects

For the case of the experimental test of Fig. 7b, the behavior of the reinforced system for different values of the FRP thickness t_{FRP} has been evaluated and compared with the experimental results whenever available, namely for $t_{FRP} =$ 0.8 mm and $t_{FRP} = 1.2$ mm. To extend the numerical analysis and identify a trend, $t_{FRP} = 0.4$ mm has also been simulated for constant beam cross section. The experimental and the numerical load vs deflections curves are reported in Fig. 13 for variable t_{FRP}. In particular, beams with thicker FRP plates exhibit higher stiffness. Both simulations and experiments detected almost the same failure load and interfacial flexural crack detachment mechanism, irrespective of the FRP thickness. However, the thicker the FRP plate, the higher the

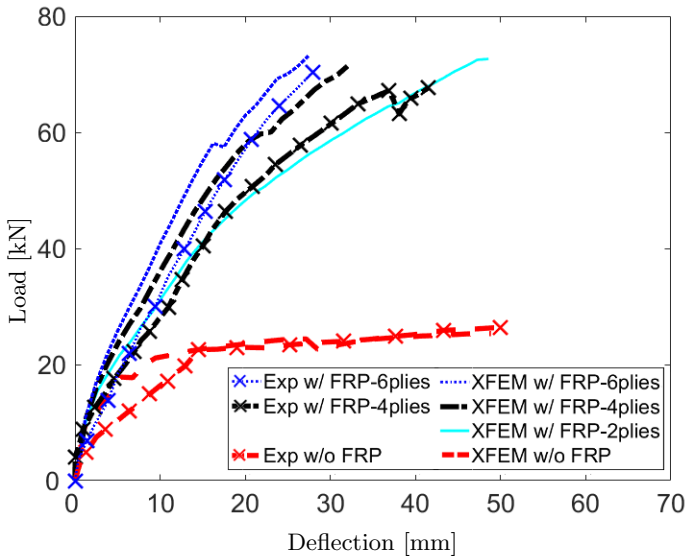

Figure 13: Comparison between experimental and numerical load-midspan-deflection curves for variable FRP plate thickness t_{FRP} and the test [8]

beam stiffness, and the more brittle the structural path. In other experimental tests [11], a similar trend was observed.

In Fig. 14, the contour plots of the damage of the steel reinforcements are reported at failure for $t_{FRP} = 1.2$ mm (a) and $t_{FRP} = 0.4$ mm (b). It can be observed that the thinner the FRP plate, the more damaged the steel rebars.

The structural influence of the width of the FRP plate has been investigated for the thick beam for the FRP widths b_{FRP} =20, 40, 80, and 120 mm. The computed load vs deflection profiles are shown in Fig. 15. It can be drawn that failure loads slightly increase with b_{FRP}. An analogous increase of the failure load with the plate width was detected in previous studies [10]. For the specimen with $b_{FRP} = 80$ mm, the numerical and the experimental maximum loads differ by the 3%. The experimental failure loads for different FRP-widths are not available.

4.2. Design loads

The current subsection suggests how to draw from the simulations an indication about the design loads and the corresponding maximum strain of the FRP

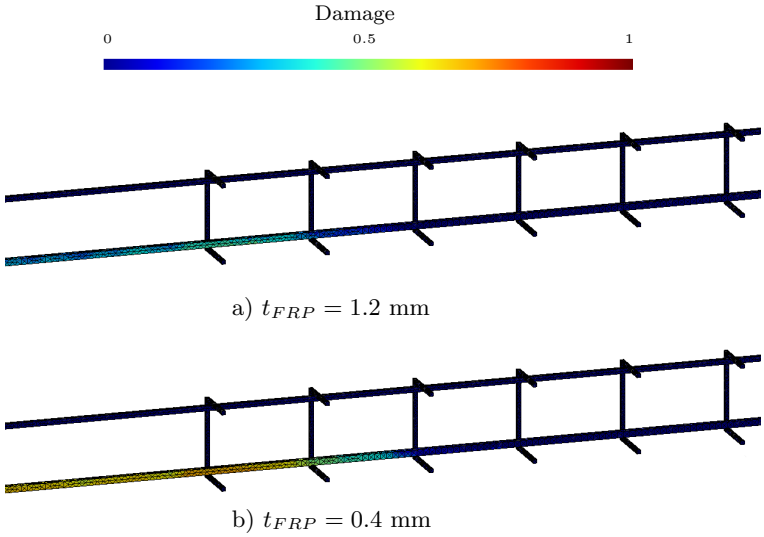

a) $t_{FRP} = 1.2$ mm

b) $t_{FRP} = 0.4$ mm

Figure 14: Comparison between the damage in the steel bars at the peak load for $t_{FRP} = 1.2$ mm (a) and $t_{FRP} = 0.4$ mm (b) for the test [7]

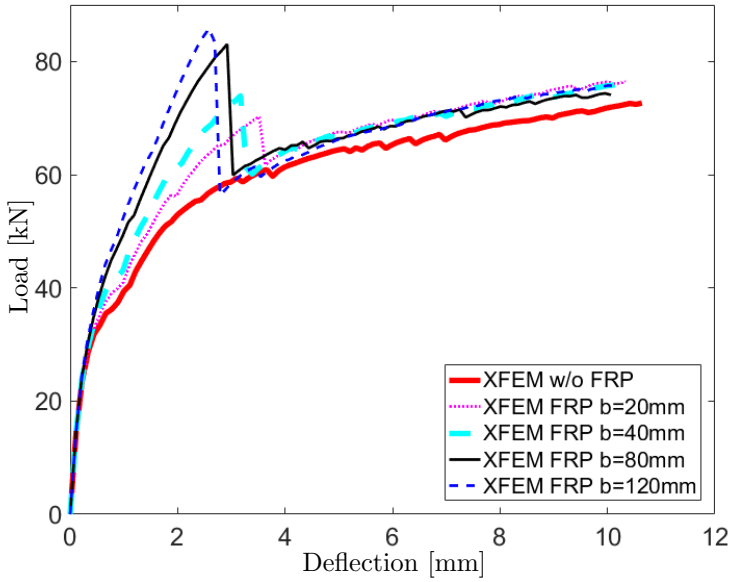

Figure 15: Load-midspan-deflection curves for variable FRP plate width b_{FRP} for the beams tested in [8]

plate for variable FRP width and thickness and constant beam cross section. To this purpose, a comparison with a reference design rule [67, 68] has been carried out. The reference design rule is detailed in the Appendix, and aims to design FRP-reinforced systems with a fair safety factor. Hence, the reference design loads have been compared to the loads detected at the occurrence of the early macro-cracks rather than to the computed failure loads.

For the thin beam [7], Fig. 16a and Fig. 16b compare the computed loads and maximum FRP strain for variable FRP-thickness t_{FRP} with the corresponding values evaluated through the reference design rule. In particular, the values computed at the occurrence of the first and second macro-crack in the concrete beam have been considered. These values are plotted with dashed lines marked with 'x' and dash-dotted lines marked with '$\square$', respectively. The reference values fall within the range of the values computed when the first and second beam macro-cracks are detected. Noteworthy, the design rule leads to design loads and FRP strains increasing for decreasing thickness of the FRP plate. This is in contrast with the present results, and with the fact that the computed and experimental failure loads have been shown to increase with t_{FRP}.

For variable width b_{FRP} and in the case of the thick beam [8], the numerical and the corresponding FRP maximum strain, evaluated at the occurrence of the first macro-crack, are displayed together with the reference values in Figs. 17a-b, respectively. In this case, the simulations are in good agreement with the design rule. In both computed and reference values, the larger the FRP plate the higher are the design loads and the smaller the FRP maximum strain.

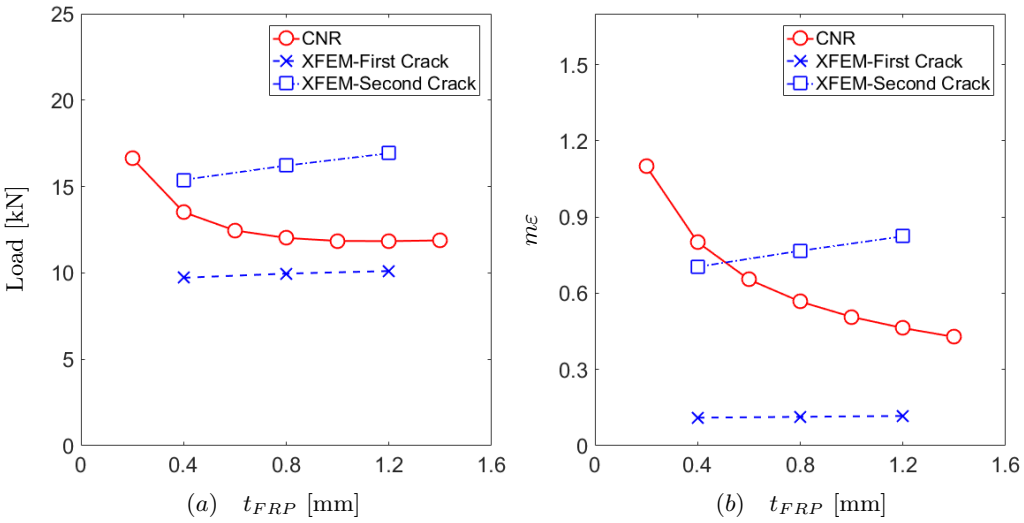

Figure 16: Comparison between numerical loads(a) and maximum FRP axial strain (b) and the design values [68] for variable thickness t_{FRP}, obtained for the thin beam tested in [7], at the occurrence of the first and second macro-crack in the concrete beam.

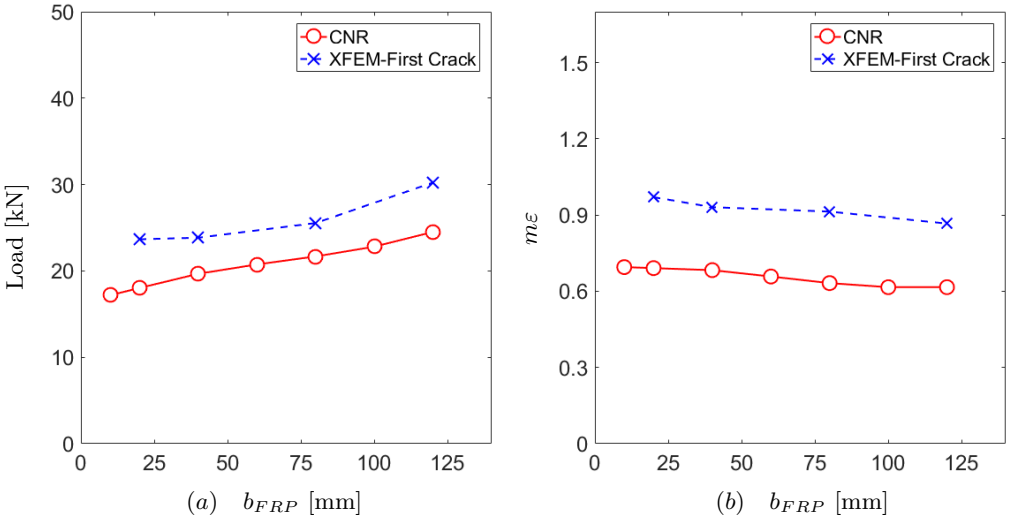

Figure 17: Comparison between numerical loads (a) and maximum FRP axial strain (b), detected at the first concrete macro-crack, and design values [68] for variable width b_{FRP} of the FRP plate, obtained for the thick beam tested in [8]

5. Discussion of the results

The present results show that, in the investigated examples, the damage process of the detachment zone above the FRP plate is triggered by the early flexural crack developing in the concrete under the load. Damage proceeds from the central part of the beam to the plate-end until the concrete cracking pattern reaches the plate end itself. Then a new damage front is activated proceeding very fast from the plate end to the center, subsequently joining the previous damage front. At this point, the FRP plate detachment is complete. In fact, either the detected structural failure is brittle, and almost simultaneous with the FRP plate detachment, or the post-detachment path joins that of the unplated beam.

As expected, the structural failure of the simulated plated beams depends on the interplay among the strengths of the concrete beam, the steel bars, and the FRP plate. In particular, the structural failure is postponed with respect to the FRP plate detachment, provided that the steel transverse reinforcement is correctly placed in the loaded region, and the yielding of the steel rebars is not complete. This is the case of the thick beam [8], having a shear span to depth ratio less than 2, where the steel reinforcements carry the load after the FRP detachment. On the contrary, in the tests by Rahimi and Hutchinson [7], with a shear span to depth ratio of about 6, the sections were adequately reinforced for the load history carried by the unplated beams, whereas they resulted under-reinforced with respect to the load levels reached by the plated beams, based on Rahimi and Hutchinson's assumption that only under-reinforced beams presumably require further reinforcements, hence the lack of stirrups at the beam center. The experimentally detected failure mode for the plated beam was shear failure followed by concrete cover separation and FRP detachment. Failure occurred suddenly, as usual in the case of shear failure of the concrete beam.

The simulations closely reproduce the experimentally detected failure mode, as proved by the fact that the computed post-failure path displays a sudden significant loss of stiffness from step C, eventually loses convergence immediately after step D, and does not join the structural path of the unplated beam. Therefore, the simulations confirm that, depending on the steel reinforcement, the strengthening effect induced by the FRP plates on under-reinforced concrete beams can change the failure mode of the unplated beam into brittle shear failure, where the FRP plate detachment follows, instead of preceding, the beam failure.

The loads computed at the first crack are not significantly sensitive to the width and thickness of the FRP plate. On the contrary, it is in the post-elastic regime that the structural behavior displays its dependency on the width and thickness of the FRP plate. In particular, the loads at which the FRP plate detaches increase with the FRP plate width, while they are not remarkably influenced by the FRP plate thickness. On the other hand, the midspan deflection at detachment increases with the thickness in all the modeled beams, though more markedly in the thin beam.

Finally, the present study suggests that the loads corresponding to the occurrence of the early macro-cracks in the concrete beams can be assumed as design loads. Such an estimate has been shown to be reasonably close to that provided by the reference design rule [68].

6. Conclusions

Numerical models that compute the structural behavior of FRP plated beams abound in the relevant literature. However, most of them require the definition of interfacial laws to be identified a priori, often lose convergence, and are unable to satisfactorily capture the concrete cracking pattern and the complete FRP

plate detachment. The proposed mechanism-based regularized XFEM overcomes the previous limitations. In fact, it requires only basic material properties and few model parameters, allows for a smooth transition from the continuum stage to the detachment stage, and models the mixed-mode fracture process zone in a physically consistent way.

It has been shown that:

- if the goal is to increase the deflection and moderately improve the detachment load, FRP plates made of two or three-plies and almost 20-40 mm wide should be used.
- Larger thicknesses and widths enhance the detachment load and reduce the ultimate deflection.
- Surprisingly, an increase of thickness and width of the FRP plate has negligible effects on the values of the midspan deflection and the load at which early cracks occur.
- Design loads increase by less than 2% when doubling the FRP plate width, and are quite constant for variable thickness.

Finally, the proposed regularized XFEM approach has consistently predicted the structural response and the crack pattern for two different four point bending tests on FRP plated reinforced concrete beams, and the procedure for transitioning from the continuous to the discontinuous regimes has been proved robust in three-dimensions.

Acknowledgments The financial support of the FAR 2016, FAR 2017, FIR 2017 funds from the University of Ferrara is gratefully acknowledged. The authors are grateful to the anonymous reviewers for helping to significantly improve the quality of the manuscript.

[1] T. Triantafillou and N. Plevris, "Strengthening of RC beams with epoxy-

bonded fibre-composite materials," *Materials and Structures*, vol. 25, pp. 201–211, 1992.

[2] L. D. Lorenzis, B. Miller, and A. Nanni, "Bond of FRP laminates to concrete," *ACI Materials Journal*, vol. 98, pp. 256–264, 2001.

[3] H. Garden and L. Hollaway, "An experimental study of the influence of plate end anchorage of carbon fibre composite plates used to strengthen reinforced concrete beams," *Composite Structures*, vol. 42, pp. 175–188, 1998.

[4] J. Teng, J. Chen, S. Smith, and L. Lam, *FRP: strengthened RC structures*. John Wiley and Sons Ltd.

[5] Y.-C. You, K.-S. Choi, and J. Kim, "An experimental investigation on flexural behavior of RC beams strengthened with prestressed CFRP strips using a durable anchorage system," *Composites Part B: Engineering*, vol. 43, pp. 3026–3036, 2012.

[6] M. Arduini, A. D. Tommaso, and A. Nanni, "Brittle failure in FRP plate and sheet bonded beams," *ACI Struct. Journal*, vol. 94, pp. 363–369, 1997.

[7] H. Rahimi and A. Hutchinson, "Concrete beams strengthened with externally bonded FRP plates," *Journal of composites for construction*, vol. 5, pp. 44–56, 2001.

[8] J. Barros, S. D. JE, and J. Lima, "Efficacy of CFRP-based techniques for the flexural and shear strengthening of concrete beams," *Cement and Concrete Composites*, vol. 29, pp. 203–217, 2007.

[9] T. Smith and J. Teng, "FRP-strengthened RC beams i: review of debonding strength models," *Engineering structures*, vol. 24, pp. 385–395, 2002.

[10] H. Thomsen, E. Spacone, S. Limkatanyu, and G. Camata, "Failure mode analyses of reinforced concrete beams strengthened in flexure with externally bonded fiber-reinforced polymers," *Journal of Composites for Construction*, vol. 8, pp. 123–131, 2004.

[11] M. Maalej and K. Leong, "Effect of beam size and FRP thickness on interfacial shear stress concentration and failure mode of FRP-strengthened beams," *Composites Science and Technology*, vol. 65, pp. 1148–1158, 2005.

[12] X. Lu, J. Teng, L. Ye, and J. Jiang, "Intermediate crack debonding in FRP-strengthened RC beams: FE analysis and strength model," *Journal of Composites for Construction*, vol. 11, pp. 161–174, 2007.

[13] M. Achintha and C. Burgoyne, "Fracture energy of the concrete–FRP interface in strengthened beams," *Engineering Fracture Mechanics*, vol. 110, pp. 38 – 51, 2013.

[14] B. Täljsten, "Strengthening of beams by plate bonding," *Journal of Materials in Civil Engineering*, vol. 9, pp. 206–212, 1997.

[15] O. Rabinovitch and Y. Frostig, "Closed-form high-order analysis of RC beams strengthened with FRP strips," *Journal of Composites for Construction*, vol. 4, pp. 65–74, 2000.

[16] X. Lu, J. Teng, L. Ye, and J. Jiang, "Bond–slip models for FRP sheets/plates bonded to concrete," *Engineering Structures*, vol. 27, pp. 920–937, 2005.

[17] P. Carrara, D. Ferretti, F. Freddi, and G. Rosati, "Shear tests of carbon fiber plates bonded to concrete with control of snap-back," *Engineering Fracture Mechanics*, vol. 78, pp. 2663–2678, 2011.

[18] E. Benvenuti, N. Orlando, D. Ferretti, and A. Tralli, "A new 3D experimentally consistent XFEM to simulate delamination in FRP-reinforced concrete," *Composites Part B: Engineering*, vol. 91, pp. 346–360, 2016.

[19] D. Ngo and A. Scordelis, "Finite element analysis of reinforced concrete beams," *Journal of the American Concrete Institute*, vol. 64, pp. 152–163, 1967.

[20] A. Ingraffea and V. Saouma, "Numerical modelling of discrete crack propagation in reinforced and plain concrete.," *In Fracture Mechanics of Concrete.*

[21] Z. Yang, J. Chen, and D. Proverbs, "Finite element modelling of concrete cover separation failure in FRP plated RC beams," *Construction and Building Materials*, vol. 17, pp. 3 – 13, 2003.

[22] G. Barenblatt, "The mathematical theory of equilibrium cracks in brittle fracture," *Advances in Applied Mechanics*, vol. 7, pp. 55–129, 1962.

[23] A. Hillerborg, M. Modeer, and P. Petersson, "Analysis of crack formation and crack growth in concrete by means of fracture mechanics and finite elements," *Cement and Concrete Research*, vol. 6, pp. 773–782, 1976.

[24] A. Needleman, "A continuum model for void nucleation by inclusion debonding," *Journal of Applied Mechanics*, vol. 54, pp. 525–531, 1987.

[25] R. D. Borst, J. Remmers, A. Needleman, and M. Abellan, "Discrete vs smeared crack models for concrete fracture: bridging the gap," *International Journal for Numerical and Analytical Methods in Geomechanics*, vol. 28, pp. 583–607, 2004.

[26] G. Chen, J. Chen, and J. Teng, "On the finite element modelling of RC

beams shear-strengthened with FRP," *Construction and Building Materials*, vol. 32, pp. 13–26, 2012.

[27] G. Chen, J. Teng, J. Chen, and Q. Xiao, "Finite element modeling of debonding failures in FRP-strengthened RC beams: A dynamic approach," *Computers and Structures*, vol. 158, pp. 167–183, 2015.

[28] Y. Rashid, "Analysis of reinforced concrete pressure vessels," *Nuclear Engineering and Design*, vol. 7, pp. 334–344, 1968.

[29] N. Pešić and K. Pilakoutas, "Concrete beams with externally bonded flexural FRP-reinforcement: analytical investigation of debonding failure," *Composites Part B: Engineering*, vol. 34, pp. 327–338, 2003.

[30] N. Kishi, G. Zhang, and H. Mikami, "Numerical cracking and debonding analysis of RC beams reinforced with FRP sheet," *Journal of Composites for Construction*, vol. 9, pp. 507–514, 2005.

[31] G. Camata, E. Spacone, and R. Zarnic, "Experimental and nonlinear finite element studies of RC beams strengthened with FRP plates," *Composites Part B: Engineering*, vol. 38, pp. 277–288, 2007.

[32] G. Chen, J. Teng, and J. Chen, "Finite-element modeling of intermediate crack debonding in FRP-plated RC beams," *Journal of Composites for Construction*, vol. 15, pp. 339–353, 2010.

[33] Z. Bazant and B. Oh, "Crack band theory for fracture of concrete," *Materieaux and Structures*, vol. 16, pp. 155–77, 1983.

[34] J. Melenk and I. Babuska, "The partition of unity finite element method: Basic theory and applications," *Computer Methods in Applied Mechanics and Engineering*, vol. 139, pp. 289–314, 1996.

[35] C. Duarte, I. Babuška, and J. Oden, "Generalized finite element methods for three-dimensional structural mechanics problems," *Computers & Structures*, vol. 77, pp. 215–232, 2000.

[36] T. Belytschko and T. Black, "Elastic crack growth in finite elements with minimal remeshing," *International Journal for Numerical Methods in Engineering*, vol. 45, pp. 601–620, 1999.

[37] T. Belytschko, N. Moës, S. Usui, and C. Parimi, "Arbitrary discontinuities in finite elements," *International Journal for Numerical Methods in Engineering*, vol. 50, pp. 993–1013, 2001.

[38] T. Belytschko, R. Gracie, and G. Ventura, "A review of extended/generalized finite element methods for material modeling," *Modelling and Simulation in Materials Science and Engineering*, vol. 17, p. 043001, 2009.

[39] N. Moës, J. Dolbow, and T. Belytschko, "A finite element method for crack growth without remeshing," *International Journal for Numerical Methods in Engineering*, vol. 46, pp. 131–150, 1999.

[40] G. Wells and L. Sluys, "A new method for modelling cohesive cracks using finite elements," *International Journal for Numerical Methods in Engineering*, vol. 50, pp. 2667–2682, 2001.

[41] E. Benvenuti, "A regularized XFEM framework for embedded cohesive interfaces," *Computer Methods in Applied Mechanics and Engineering*, vol. 197, pp. 4367–4378, 2008.

[42] Y. Wang and H. Waisman, "Progressive delamination analysis of composite materials using XFEM and a discrete damage zone model," *Computational Mechanics*, vol. 55, pp. 1–26, 2015.

[43] E. Benvenuti, G. Ventura, N. Ponara, and A. Tralli, "Variationally consistent extended fe model for 3D planar and curved imperfect interfaces," *Computer Methods in Applied Mechanics and Engineering*, vol. 267, pp. 434–457, 2013.

[44] E. Benvenuti, "XFEM with equivalent eigenstrain for matrix–inclusion interfaces," *Computational Mechanics*, vol. 53, pp. 893–908, 2014.

[45] G. Pijaudier-Cabot and Z. Bažant, "Nonlocal damage theory," *Journal of Engineering Mechanics*, vol. 113, pp. 1512–1533, 1987.

[46] R. Peerlings, M. Geers, R. de Borst, and W. Brekelmans, "A critical comparison of nonlocal and gradient-enhanced softening continua," *International Journal of Solids and Structures*, vol. 38, pp. 7723 – 7746, 2001.

[47] E. Benvenuti, G. Borino, and A. Tralli, "A thermodynamically consistent nonlocal formulation for damaging materials," *European Journal of Mechanics - A Solids*, vol. 21, pp. 535–553, 2002.

[48] E. Benvenuti and N. Orlando, "Failure of FRP-strengthened SFRC beams through an effective mechanism-based regularized XFEM framework," *Composite Structures*, vol. 172, pp. 345–358, 2017.

[49] E. Iarve, M. Gurvich, and D. Mollenhauer, "Mechanism-based direct simulation of tensile failure in composite laminates," in *51st AIAA/ASME/ASCE/AHS/ASC Structures, Structural Dynamics, and Materials Conference. Orlando, Florida*, 2010.

[50] K. Hoos, E. Iarve, M. Braginsky, E. Zhou, and D. Mollenhauer, "Static strength prediction in laminated composites by using discrete damage modeling," *Journal of Composite Materials*, vol. 51, pp. 1473–1492, 2017.

[51] E. Dror and O. Rabinovitch, "Size effect in the debonding failure of FRP strengthened beams," *Engineering Fracture Mechanics*, vol. 165, pp. 161–181, 2016.

[52] E. Benvenuti, O. Vitarelli, and A. Tralli, "Delamination of FRP-reinforced concrete by means of an extended finite element formulation," *Composites Part B: Engineering*, vol. 43, pp. 3258–3269, 2012.

[53] T. Fries and T. Belytschko, "The extended/generalized finite element method: An overview of the method and its applications," *International Journal for Numerical Methods in Engineering*, vol. 84, pp. 253–304, 2010.

[54] J. Gálvez, M. Elices, G. Guinea, and J. Planas, "Mixed mode fracture of concrete under proportional and nonproportional loading," *International Journal of Fracture*, vol. 94, pp. 267–284, 1998.

[55] Z. Bažant and P. Pfeiffer, "Shear fracture tests of concrete," *Matériaux et Constructions*, vol. 19, pp. 111–121, 1986.

[56] S. Osher and J. Sethian, "Fronts propagating with curvature dependent speed: Algorithms based on hamilton-jacobi formulations," *Journal of Computational Physics*, vol. 79, pp. 12–49, 1988.

[57] E. Benvenuti, G. Ventura, N. Ponara, and A. Tralli, "Accuracy of three-dimensional analysis of regularized singularities," *International Journal for Numerical Methods in Engineering*, vol. 101, pp. 29–53, 2015.

[58] E. Benvenuti, "Mesh–size–objective XFEM for regularized continuous–discontinuous transition," *Finite Elements in Analysis and Design*, vol. 47, pp. 1326–1336, 2011.

[59] E. Benvenuti and A. Tralli, "Simulation of finite-width process zone in

concrete-like materials by means of a regularized extended finite element model," *Computational Mechanics*, vol. 50, pp. 479–497, 2012.

[60] E. Benvenuti, "Damage integration in the strain space," *International Journal of Solids and Structures*, vol. 41, pp. 3167–3191, 2004.

[61] M. Cervera, M. Chiumenti, and R. Codina, "Mixed stabilized finite element methods in nonlinear solid mechanics. part ii: Strain localization," *Computer Method in Applied Mechanics and Engineering*, vol. 199, pp. 2571–2589, 2010.

[62] J. Lemaitre, "A continuous damage mechanics model for ductile fracture," *Transactions of the ASME Journal of Engineering Materials and Technology*, vol. 107, pp. 83–89, 1985.

[63] W. Ramberg and W. Osgood, "Description of stress-strain curves by three parameters," *Technical notes. Washington D.C: National Advisory Committee for Aeronautics*, no. 902, pp. 1–29, 1943.

[64] G. Ventura and E. Benvenuti, "Equivalent polynomials for quadrature in heaviside function enriched elements," *International Journal for Numerical Methods in Engineering*, vol. 102, pp. 688–710, 2015.

[65] NTC08, "Norme tecniche per le costruzioni in zone sismiche," *Ministerial Decree DM*, vol. 14, no. 08, pp. 9–04, 2008.

[66] K. Subramaniam, C. Carloni, and L. Nobile, "Width effect in the interface fracture during shear debonding of FRP sheets from concrete," *Engineering Fracture Mechanics*, vol. 74, pp. 578–594, 2007.

[67] FIB, "Externally bonded FRP reinforcement for RC structures," *Bulletin Fédération Internationale Du Béton*, no. 14, pp. 1–138, 2001.

[68] CNR, " CNR 200/2004: Guide for the Design and Construction of Externally Bonded FRP Systems for Strengthening Existing Structures," 2004.

Appendix The CNR design rules [68] are based on the CEB-FIP code [67] and the following hypotheses: cross-beam section plane and perpendicular to the beam axis after deflection; perfect bond between FRP and concrete, and steel and concrete; concrete as a no-tension material; FRP linear elastic up to the failure; failure due either to concrete crushing or to FRP tensile rupture For plate end debonding failure, the ultimate design strength is

$$f_{dd} = \frac{1}{\gamma_{f,d}\sqrt{\gamma_c}}\sqrt{\frac{2\,E_{FRP}\,\Gamma_{Fk}}{t_f}}\,, \tag{.1}$$

where $\gamma_{f,d}$ and γ_c are the safety partial factor, E_{FRP} is the Young modulus of the FRP reinforcement and Γ_{Fk} is the specific fracture energy of the FRP-concrete interface. The specific fracture energy can be expressed as $\Gamma_{Fk} = 0.03\,k_b\sqrt{f_{ck}\,f_{ctm}}$, where

$$k_b = \sqrt{\frac{2-\frac{b_{FRP}}{b}}{1+\frac{b_{FRP}}{400}}} \geq 1 \qquad \frac{b_{FRP}}{b} \geq 0.33 \tag{.2}$$

depends on the geometry of the FRP reinforced system. Finally, f_{ck} and f_{ctm} are the characteristic compressive strength and the mean tensile strength of the concrete, respectively. For $l_{FRP} \leq l_e$, where $l_e = \sqrt{\frac{E_{FRP}\,t_{FRP}}{2\,f_{ctm}}}$ is the optimal bonded length namely the shorter length of the FRP bonded area that allows the maximum force transfer between concrete and FRP, the ultimate strength has to be reduced according to

$$f_{dd,rid} = f_{dd}\,\frac{l_{FRP}}{l_e}\left(2-\frac{l_{FRP}}{l_e}\right). \tag{.3}$$

For flexural intermediate debonding failure, the design rule specifies the ultimate

design strength as $f_{dd,2} = k_{cr}\ f_{dd}$ where $k_{cr} = 3$.